



Cite this: *Catal. Sci. Technol.*, 2021,  
11, 943

# Amorphous $\text{Co}_3\text{S}_4$ nanoparticle-modified tubular $\text{g-C}_3\text{N}_4$ forms step-scheme heterojunctions for photocatalytic hydrogen production†

Yuanpeng Wang,<sup>abc</sup> Xuqiang Hao,<sup>abc</sup> Lijun Zhang,<sup>abc</sup>  
Zhiliang Jin <sup>\*abcd</sup> and Tiansheng Zhao <sup>\*d</sup>

An effective method to reduce the recombination rate of photogenerated electron-hole pairs was developed by the construction of heterojunctions with rationally designed photocatalysts having a matched band structure. Herein,  $\text{g-C}_3\text{N}_4$  hexagonal tubes possessing a lower conduction band were coupled with  $\text{Co}_3\text{S}_4$  ultra-fine nanoparticles having relatively higher positions for their conduction band. A step-scheme heterojunction was constructed between these two materials, and through this heterojunction, the spatial charge separation was boosted. The boosted spatial charge separation led to more useful electrons with a higher reduction ability that participated in a photocatalytic  $\text{H}_2$  evolution reaction. The  $\text{Co}_3\text{S}_4$  ultra-fine nanoparticles act as a mirror to repeatedly scatter and reflect incident light and thus enhance light utilization, and they also accelerate the spatial charge separation. The photocatalytic  $\text{H}_2$  evolution activity of the composite catalyst reached  $2120 \mu\text{mol g}^{-1} \text{h}^{-1}$ , which was 176 times higher than that of pristine  $\text{g-C}_3\text{N}_4$  tubes. A series of characteristics were determined to investigate the interaction that occurred between the  $\text{g-C}_3\text{N}_4$  hexagonal tubes and the  $\text{Co}_3\text{S}_4$  ultra-fine nanoparticles, and to study the mechanism of the formed step-scheme. This work will guide the design of step-scheme heterojunction-based photocatalysts to produce  $\text{H}_2$  from photocatalytic water splitting.

Received 13th October 2020,  
Accepted 18th November 2020

DOI: 10.1039/d0cy02009e

rsc.li/catalysis

## 1. Introduction

The energy shortage and crisis have severely restricted sustainable development. Hydrogen ( $\text{H}_2$ ) is a clean and environmentally friendly energy that can be produced from photocatalytic water splitting using inexhaustible solar energy, and hydrogen has been regarded as a promising renewable energy to meet the energy shortage and crisis.<sup>1,2</sup> Therefore, there has been an intense effort to discover an inexpensive, stable, and robust photocatalyst. Many photocatalysts such as metal-contained catalysts<sup>3–14</sup> and graphdiyne (GD)<sup>15–17</sup> or new members of carbon families or other metal-free catalysts<sup>18</sup> have been widely researched.  $\text{g-C}_3\text{N}_4$

is a new member of photocatalysts that is metal-free and shows great prospect in practical applications because it was first applied to produce  $\text{H}_2$  from water splitting by photocatalysis.<sup>19</sup> Even though it possesses high thermal and chemical stability and it is a metal-free photocatalyst that can be easily obtained, bulk  $\text{g-C}_3\text{N}_4$  is subjected to intrinsic drawbacks, such as low specific surface area, and severe recombination of photo-generated electron-hole pairs.<sup>20,21</sup> Therefore, ongoing efforts have been devoted to solve these problems by resolving the deficiencies of bulk  $\text{g-C}_3\text{N}_4$ . Acquiring unique morphology and structure by adjusting synthetic methodologies will increase the specific surface area or make some adjustment to the band structure of  $\text{g-C}_3\text{N}_4$  and increase the transfer efficiency of electron-holes in  $\text{g-C}_3\text{N}_4$ . Thus far, a host of different morphologies of  $\text{g-C}_3\text{N}_4$ , such as nanorods,<sup>22</sup> seaweeds,<sup>23</sup> nanosheets<sup>24</sup> and tubular  $\text{g-C}_3\text{N}_4$  (ref. 25–28) have been rationally designed to increase the light harvesting ability of  $\text{g-C}_3\text{N}_4$  or to adjust its band structure to overcome the intrinsic drawbacks of bulk  $\text{g-C}_3\text{N}_4$ . Surprisingly, results can be obtained by constructing a certain morphology of photocatalysts. For instance,  $\text{g-C}_3\text{N}_4$  with a nanotube shape can contribute a large specific surface area to provide a large number of active sites, and it also shortens the transfer distance of photo-induced carriers in  $\text{g-C}_3\text{N}_4$  from

<sup>a</sup> School of Chemistry and Chemical Engineering, North Minzu University, Yinchuan 750021, P.R. China. E-mail: zl-jin@nmu.edu.cn

<sup>b</sup> Ningxia Key Laboratory of Solar Chemical Conversion Technology, North Minzu University, Yinchuan 750021, P.R. China

<sup>c</sup> Key Laboratory for Chemical Engineering and Technology, State Ethnic Affairs Commission, North Minzu University, Yinchuan 750021, P.R. China

<sup>d</sup> State Key Laboratory of High-efficiency Utilization of Coal and Green Chemical Engineering, Ningxia University, Yinchuan, 750021, P.R. China.

E-mail: zhaots@nxu.edu.cn

† Electronic supplementary information (ESI) available. See DOI: 10.1039/d0cy02009e

the phase to its surface. In addition, tubular  $g\text{-C}_3\text{N}_4$  with a hollow structure can enhance light absorption and increase the separation and transfer kinetics of photo-generated charge carriers by the multiple light scattering/reflection effect in the inner cavity of  $g\text{-C}_3\text{N}_4$ .

Even though the different morphologies of  $g\text{-C}_3\text{N}_4$  are rationally designed and all of them exhibit increased photocatalytic performance, the synthesis methods are time-consuming, expensive, and require hazardous reagents that are harmful to environment in the process of removing the template. Certain structured micro- or nano-materials are designed and obtained by treating supermolecular precursors that self-assemble through hydrogen bonding among molecules, and these materials are applied to many fields such as photocatalysis because the hydrogen bonding possesses features of strong direction and saturation.<sup>29,30</sup> It is well known that using water as the solvent in the process of synthesis is more beneficial for the self-assembly of molecules based on hydrogen bonding because they can acquire precursors that are stable and large. Additionally, there are quite a few advantages such as inexpensive, easily

obtained, and environmentally friendly when choosing water as the solvent to obtain supermolecular precursors.

In this work,  $g\text{-C}_3\text{N}_4$  with a tubular shape was fabricated by choosing deionized water as the solvent to synthesize supermolecular precursors and then calcine the precursors. Then, ultrafine  $\text{Co}_3\text{S}_4$  nanoparticles were anchored on the surface of tubular  $g\text{-C}_3\text{N}_4$  as cocatalyst to enhance the photocatalytic performance of  $g\text{-C}_3\text{N}_4$ . The results of emission scanning electron microscopy and transmission electron microscopy showed that the supermolecular precursors derived from melamine formed hollow  $g\text{-C}_3\text{N}_4$  tubes, and ultrafine  $\text{Co}_3\text{S}_4$  nanoparticles were distributed on the surface of the  $g\text{-C}_3\text{N}_4$  tubes. The hollow structure enhances the light absorbed by  $g\text{-C}_3\text{N}_4$ , which is beneficial for the multiple light scattering/reflection effect in the inner cavity of  $g\text{-C}_3\text{N}_4$ . Even though the multiple light scattering/reflection effect in the inner cavity of  $g\text{-C}_3\text{N}_4$  enhances its light absorption, light utilization is still inefficient in the outward wall because light entering into the tube can be utilized on both tails of the tube. The ultrafine  $\text{Co}_3\text{S}_4$  nanoparticles distributed on the surface of the tube alter the relatively smooth surface of  $g\text{-C}_3\text{N}_4$ .

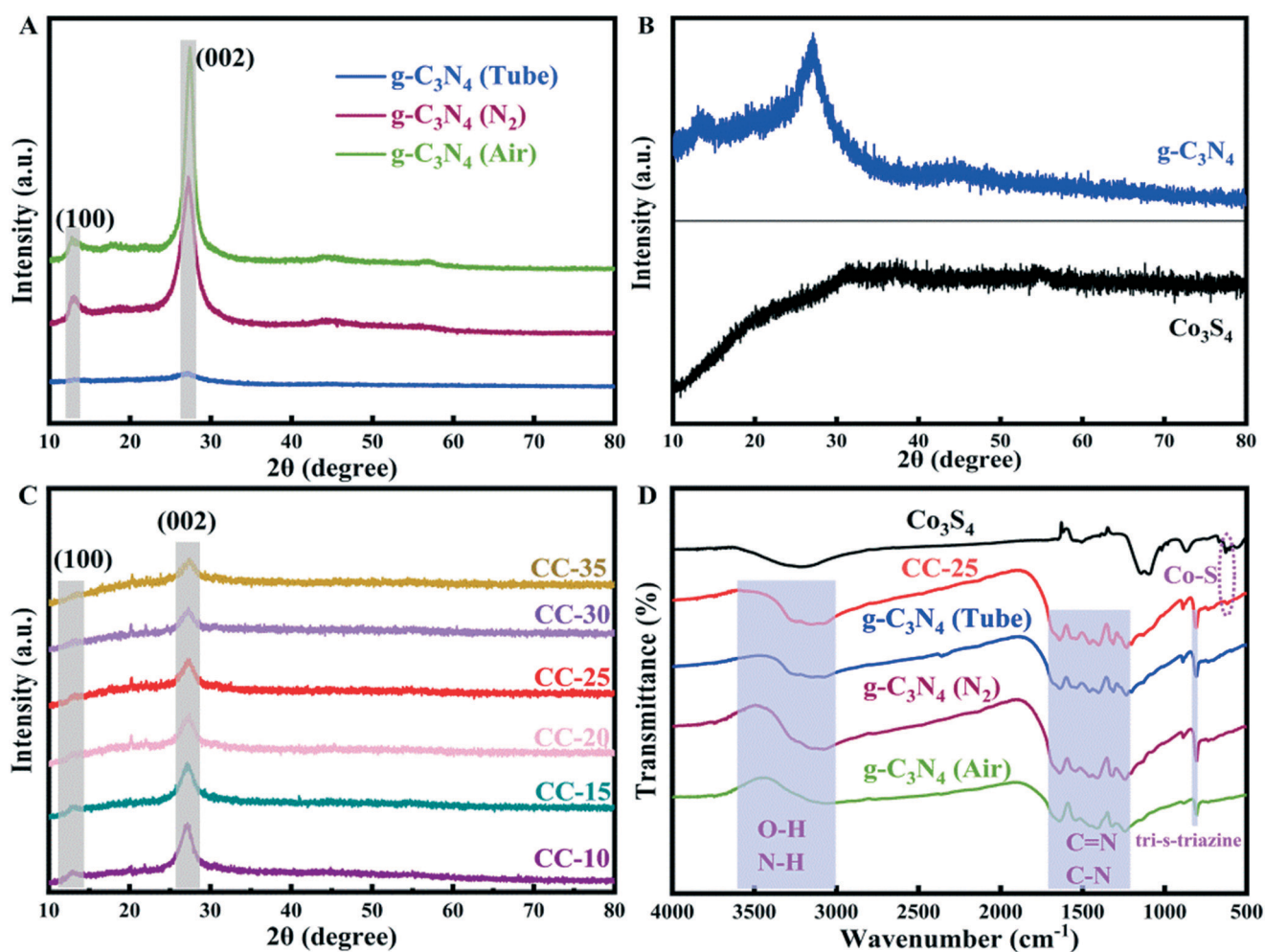


Fig. 1 XRD patterns of (A)  $g\text{-C}_3\text{N}_4$  (prepared using different methods), (B)  $\text{Co}_3\text{S}_4$  and  $g\text{-C}_3\text{N}_4$  tube, (C) CC- $x$  ( $x = 10, 15, 20, 25, 30, 35$ ), and (D) FT-IR spectra of  $g\text{-C}_3\text{N}_4$  (prepared using different methods),  $\text{Co}_3\text{S}_4$ , and CC-25.

$C_3N_4$  so that it becomes uneven, resulting in the same scattering/reflection effect. The scattering/reflection effect occurring on the surface of  $g-C_3N_4$  can enhance light utilization because ultrafine  $Co_3S_4$  nanoparticles can act as a hole in an uneven mirror to scatter and reflect light irradiating to the surface of  $Co_3S_4$  nanoparticles, and some light can be reflected to the surface of the  $g-C_3N_4$  tube, which is the reason for the enhanced light absorption of  $g-C_3N_4$ .

## 2. Results and discussion

### 2.1 Structural and morphological analysis

**2.1.1 XRD and FTIR analysis.** Fig. 1A shows XRD patterns of  $g-C_3N_4$  synthesized using different methods, from which it can be seen that the tubular  $g-C_3N_4$  maintains the two characteristic peaks of  $g-C_3N_4$ . The two peaks are centered at approximately  $13.1^\circ$  and  $27.2^\circ$ , as previously reported. These two peaks can be assigned to the (100) and (002), with the former one indexed to the in-plane structural packing motif, and the latter to the periodic stacking of layers along the  $c$ -axis.<sup>31</sup> The XRD pattern of  $Co_3S_4$  presented in Fig. 1B exhibits no obvious diffraction peak due to its amorphous characteristics, which also can be confirmed by the results of

HRTEM of CC-25. XRD patterns of CC- $x$  ( $x = 10, 15, 20, 25, 30, 35$ ) are shown in Fig. 1C, and no diffraction peaks of  $Co_3S_4$  can be found in these patterns, which occurs due to the amorphous characteristics of  $Co_3S_4$  ultrafine nanoparticles in comparison to tubular  $g-C_3N_4$ , and this can be observed from Fig. 1B.

The chemical structures of  $g-C_3N_4$  (synthesized with different methods),  $Co_3S_4$ , and CC-25 were analyzed employing the FT-IR spectra presented in Fig. 1D. The tubular  $g-C_3N_4$  synthesized with a two-step hydrothermal method maintained a core structure that is similar to that of bulk  $g-C_3N_4$  (prepared in air and nitrogen). The absorption band located at approximately  $807\text{ cm}^{-1}$  can be assigned to the tri-*s*-triazine unit,<sup>26</sup> which indicates a complete skeleton  $g$ -structure of  $g-C_3N_4$ . The absorption peaks located from  $1200$  to  $1700\text{ cm}^{-1}$  are indexed to the C=N and C-N stretching vibration modes.<sup>32,33</sup> The weak absorption peaks situated in the range from  $3000$  to  $3600\text{ cm}^{-1}$  are the O-H and N-H stretching vibration modes.<sup>34</sup> FTIR spectroscopy of  $Co_3S_4$  shows a weak absorption peak that is centered at approximately  $620\text{ cm}^{-1}$ , and it can be indexed to the stretching vibrations of cobalt-sulphur bonds.<sup>35,36</sup> In addition, the absorption peak of cobalt-sulphur bonds can

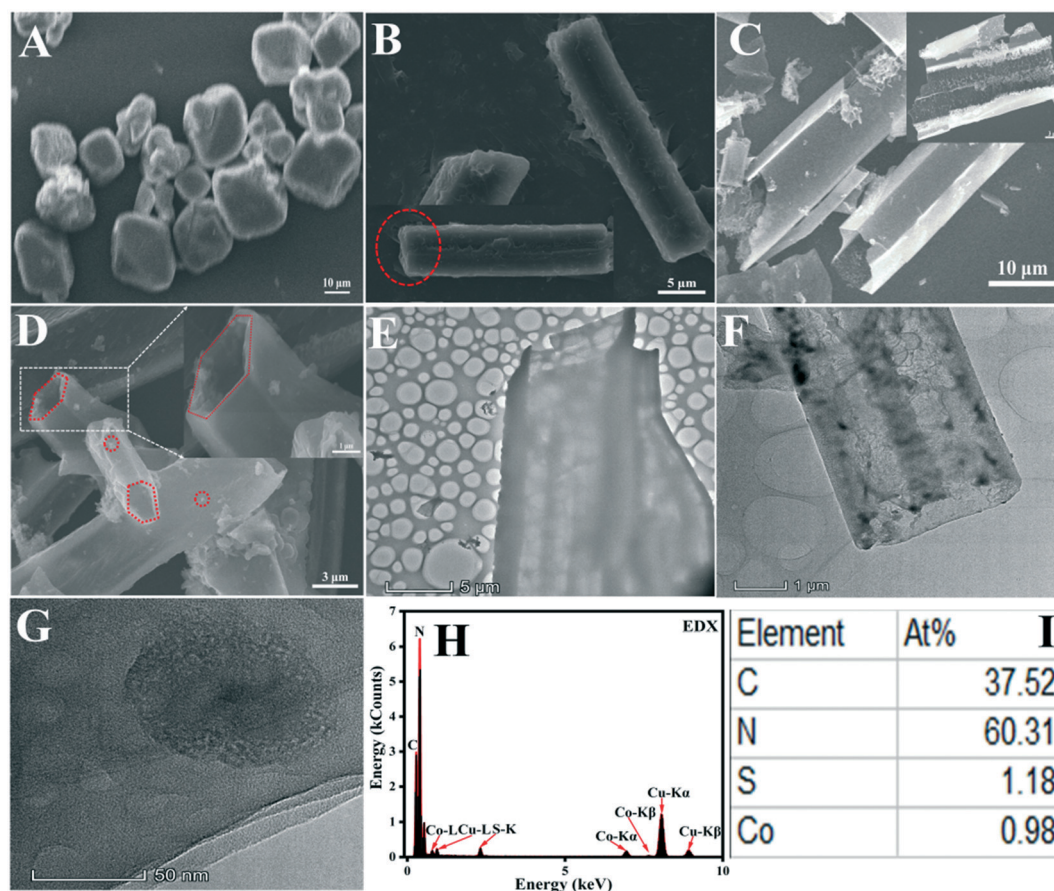


**Fig. 2** SEM images of (A) melamine raw material, (B) supramolecular precursor prepared by the hydrothermal method with melamine as the raw material, (C)  $g-C_3N_4$  tubes, (D) CC-25. TEM images of (E)  $g-C_3N_4$  tubes and (F) CC-25. HRTEM image of (G) CC-25. (H) EDX image of CC-25. (I) The atomic fractions of C, N, S, and Co.

be found in the FTIR pattern of CC-25, which indicates that  $g\text{-C}_3\text{N}_4$  tubes and  $\text{Co}_3\text{S}_4$  nanoparticles were successfully combined, and this can also be proved by the EDX results.

**2.1.2 SEM and TEM analysis.** The SEM image shows the supramolecular precursor prepared by a hydrothermal method with melamine as raw materials. It can be seen from the SEM image of melamine (presented in Fig. 2A) without any treatment that its morphology is totally different from those of the supramolecular precursors and  $g\text{-C}_3\text{N}_4$  tubes. Fig. 2B is an SEM image of supramolecular precursors with a hexagonal morphology but not hollow structure. When the precursors were treated in a  $\text{N}_2$  atmosphere, the morphology changed to hexagonal tubes with weak walls. Fig. 2D displays SEM images of CC-25 with different resolution, and it can be clearly seen that  $g\text{-C}_3\text{N}_4$  exhibits the apparent morphology of hexagonal tubes and some irregular and relatively large points assembled by ultrafine  $\text{Co}_3\text{S}_4$  nanoparticles on the surface of these tubes. These assembled  $\text{Co}_3\text{S}_4$  nanoparticles on the surface of  $g\text{-C}_3\text{N}_4$  tubes can act as a mirror to reflect and scatter light incident to the surface of the tubes, which is beneficial for photocatalytic hydrogen evolution. The ultrafine  $\text{Co}_3\text{S}_4$  nanoparticles are distributed on different surfaces of these tubes, and some are

distributed on the junction of two surfaces.  $\text{Co}_3\text{S}_4$  nanoparticles on the ridge will reflect incident light from one surface to another, and the utilization of incident light will be enhanced through this phenomenon (a schematic diagram of the scatter process is shown in Scheme S2A<sup>†</sup>). The SEM image presented in Fig. 2C and TEM image of pristine  $g\text{-C}_3\text{N}_4$  shown in Fig. 2E illustrate its hollow structure and weak walls. The TEM images of CC-25 displayed in Fig. 2F and G show that some areas are opaque because they are occupied by many congregated ultrafine  $\text{Co}_3\text{S}_4$  nanoparticles. As claimed in the section on  $\text{H}_2$  evolution performance, a suitable loading amount of  $\text{Co}_3\text{S}_4$  nanoparticles can maximally enhance the photocatalytic hydrogen performance (shown in Scheme S2B<sup>†</sup>). Most areas will be occupied when loading too many  $\text{Co}_3\text{S}_4$  nanoparticles on the surface of  $g\text{-C}_3\text{N}_4$  tubes, and this phenomenon will result in low utilization on surface areas because excessive  $\text{Co}_3\text{S}_4$  nanoparticles will hinder incident light from reaching the surface of the  $g\text{-C}_3\text{N}_4$  tubes (as shown in Scheme S2C<sup>†</sup>). The TEM DEX results (Fig. 2H) confirm the presence of elements C, N, S, and Co in CC-25. The atomic fraction (Fig. 2I) from the EDX results also reveals that the ratios of C/N and Co/S are similar to the ratios in  $g\text{-C}_3\text{N}_4$  and  $\text{Co}_3\text{S}_4$ .

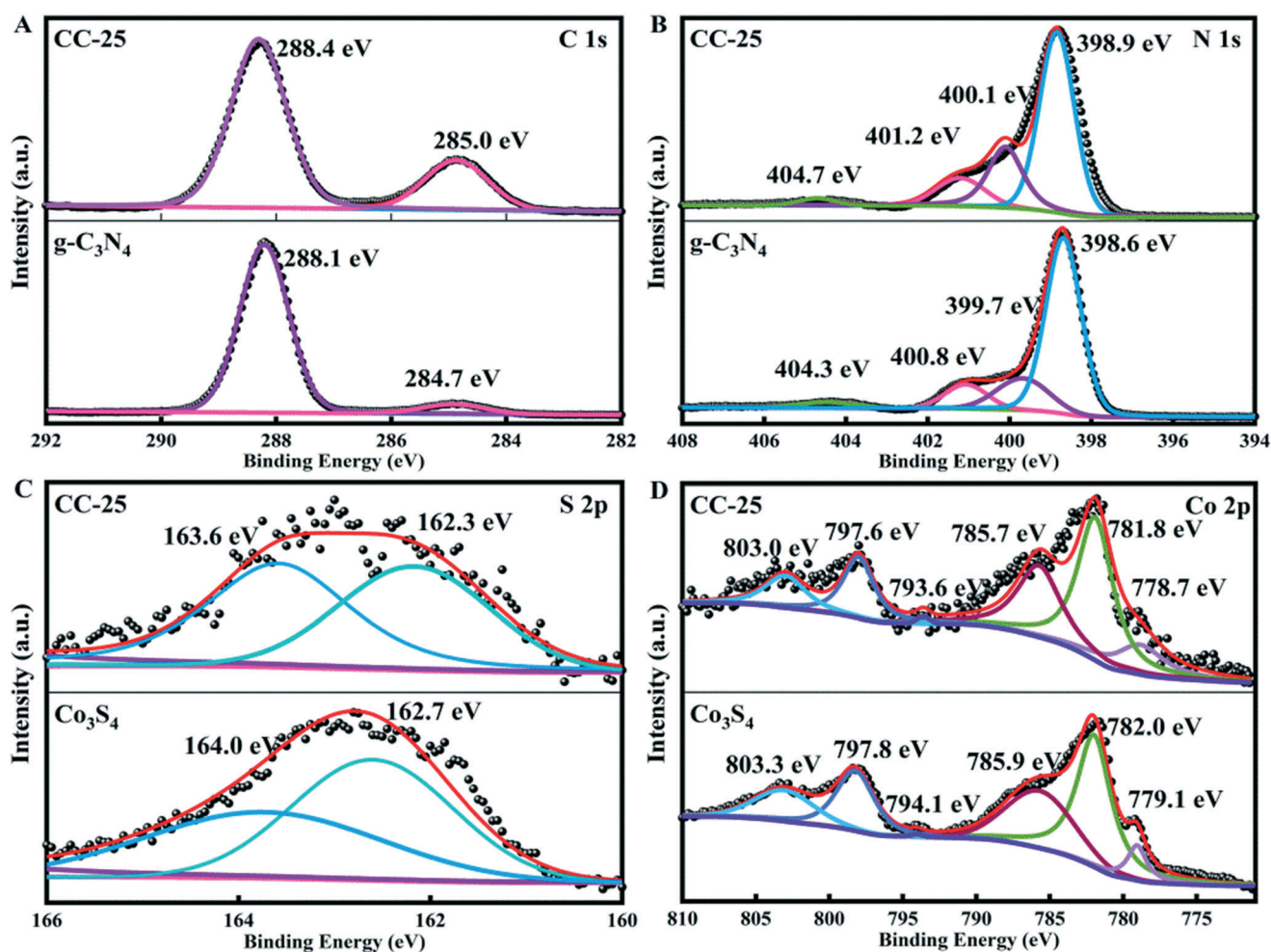


Fig. 3 High resolution XPS spectra of (A) C 1s, (B) N 1s, (C) S 2p, and (D) Co 2p.

**2.1.3 XPS analysis.** The transfer direction of electrons and the surface chemical valence states of elements were studied by carrying out X-ray photoelectron spectroscopy (XPS). The XPS survey spectra of g-C<sub>3</sub>N<sub>4</sub>, Co<sub>3</sub>S<sub>4</sub>, and CC-25 are presented in Fig. S1.† Fig. 3A shows the high-resolution XPS spectrum of C 1s. The two peaks with binding energies of 284.7 and 288.4 eV can be indexed to the carbon atoms in the N=C (-N)<sub>2</sub> group and the graphitic adventitious C=C/C-C bond in g-C<sub>3</sub>N<sub>4</sub>.<sup>37</sup> The high-resolution XPS spectrum of N 1s (Fig. 3B) can be deconvoluted into four peaks, and these peaks with bonding energies of 404.3, 400.8, 399.7, and 398.6 eV can be indexed to  $\pi$  excitation of the C=N, C-N-H, N-(C)<sub>3</sub>, and C-N=C conjugated structures in g-C<sub>3</sub>N<sub>4</sub>, respectively.<sup>38</sup> There are two peaks with binding energies of 162.7 and 164.0 in the spectrum of S 2p (Fig. 3C), and the two peaks can be indexed to S (-II) in sulfide (CoS<sub>x</sub>).<sup>39</sup> The high-resolution XPS spectrum of Co 2p presented in Fig. 3D contains six peaks. Those peaks with binding energies of 779.1 and 794.1 eV belong to Co 2p<sub>3/2</sub> and Co 2p<sub>1/2</sub>, which are attributed to Co<sup>2+</sup>. The peaks centered at 782.0 and 797.8 eV can be assigned to Co 2p<sub>3/2</sub> and Co 2p<sub>1/2</sub>, and

indicate the existence of Co<sup>3+</sup>.<sup>40–42</sup> The other two peaks with binding energies of 785.9 and 803.3 eV belong to satellites.<sup>41</sup> In addition, the spectra of C 1s, N 1s, S 2p, and Co 2p of CC-25 were obtained, and the results are shown in Fig. 3. All binding energies of C 1s and N 1s in CC-25 shift towards higher energy, and binding energies of S 2p and Co 2p in CC-25 shift towards lower energy, which indicates that electrons are transferred from g-C<sub>3</sub>N<sub>4</sub> tubes to Co<sub>3</sub>S<sub>4</sub> ultrafine nanoparticles.

**2.1.4 BET analysis.** The pore structures of the two pristine samples and the composite were analyzed by conducting N<sub>2</sub> adsorption–desorption isotherms and pore size distribution analysis, as shown in Fig. 4. Fig. 4A shows that all three samples exhibited type IV isotherms with H3 hysteresis loops at the relative pressure ( $P/P_0$ ) ranging from 0 to 1, which is indicative of the presence of mesopores.<sup>15</sup> The inset image in Fig. 4A shows that the average diameters of these samples are mainly from 2 to 50 nm, which also indicates the presence of mesopores. Fig. 4B–D illustrates the detailed adsorption–desorption isotherms and corresponding pore size distribution (inset pictures), in which the isotherms of g-

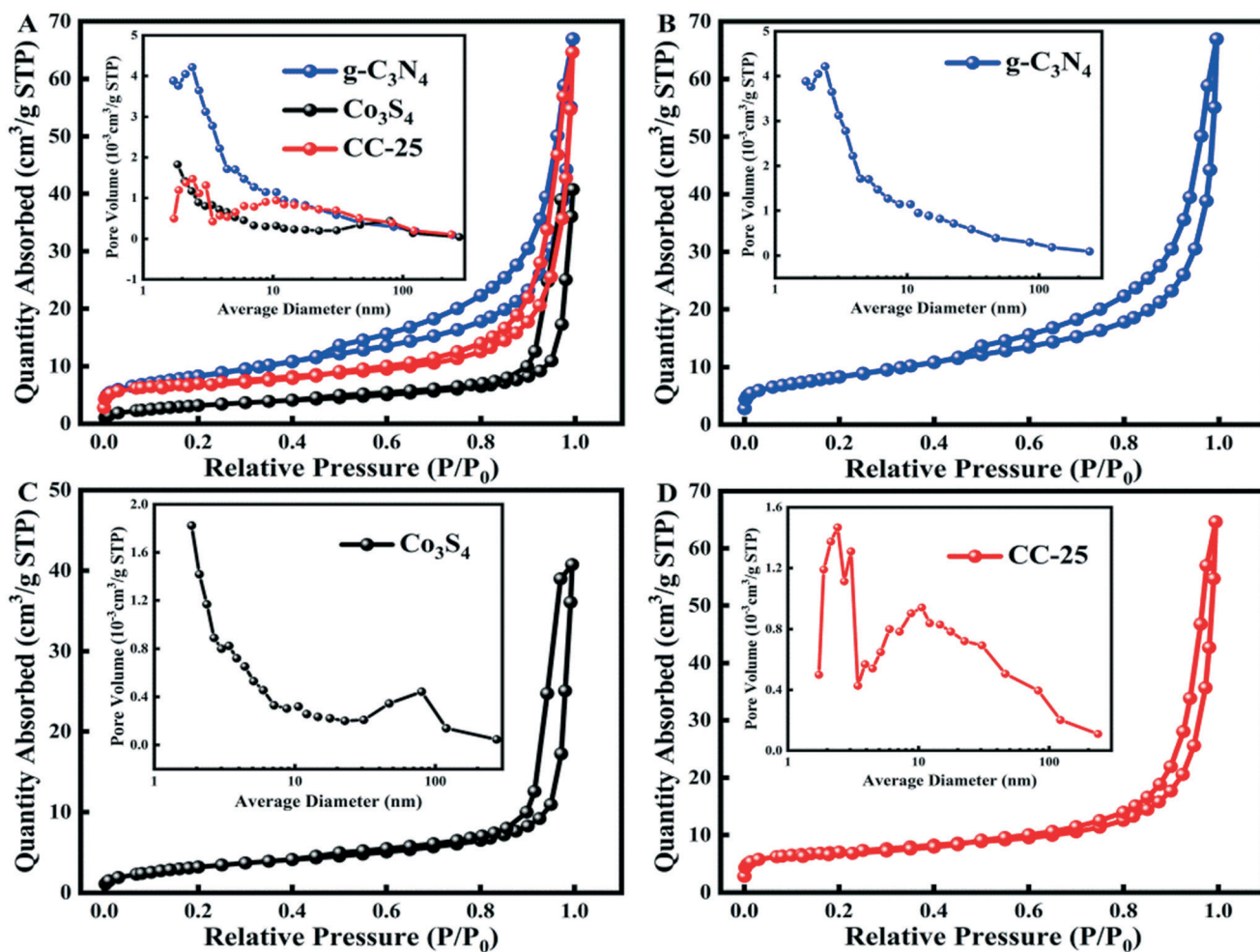


Fig. 4 (A) N<sub>2</sub> adsorption–desorption isotherms for g-C<sub>3</sub>N<sub>4</sub> tubes, Co<sub>3</sub>S<sub>4</sub>, and CC-25, and corresponding pore size distribution curves (inset). (B)–(D) N<sub>2</sub> adsorption–desorption isotherms for g-C<sub>3</sub>N<sub>4</sub> tubes, Co<sub>3</sub>S<sub>4</sub>, and CC-25, and corresponding pore size distribution curves (inset).

$C_3N_4$  tubes,  $Co_3S_4$ , and CC-25 exhibit bi-model pore size distributions, which are indicative of mesoporous structures for these samples. In addition, the hybrid exhibits the characteristics of both  $g-C_3N_4$  tubes and  $Co_3S_4$ , demonstrating that the two materials are successfully coupled. The BET specific surface area ( $S_{BET}$ ) of CC-25 ( $22 \text{ m}^2 \text{ g}^{-1}$ ) is slightly lower than that of pristine  $g-C_3N_4$ , which indicates that the BET specific surface area is not the main factor that affects the photocatalytic  $H_2$  evolution activity. The decrease in the  $S_{BET}$  of the composite can be attributed to many accumulated  $Co_3S_4$  nanoparticles that occupy the surface area of the hexagonal  $g-C_3N_4$  tubes, resulting in a decrease in the  $S_{BET}$  of CC-25. The hexagonal  $g-C_3N_4$  tubes with a larger  $S_{BET}$  can provide a larger surface area to anchor more  $Co_3S_4$  nanoparticles and prevent these nanoparticles from accumulating while also providing additional sites for photocatalytic reactions (Table 1).

## 2.2 Optical absorption properties

The photocatalytic performance is affected to some extent by the optical absorption properties of catalysts. Fig. 5A shows the optical properties of bulk  $g-C_3N_4$  prepared by calcining melamine in air (denoted as  $g-C_3N_4$  (air)), bulk  $g-C_3N_4$  prepared by calcining melamine in  $N_2$  atmosphere (denoted as  $g-C_3N_4$  ( $N_2$ )), and tubular  $g-C_3N_4$ . The absorption edge and the absorbance of the tubular  $g-C_3N_4$  were lower than those of the two bulk- $g-C_3N_4$  samples when lower than 430 nm in the visible light region. However, the absorption edge of the  $g-C_3N_4$  tubes shifts to a longer wavelength, and the absorbance becomes stronger than that of the counterparts of bulk  $g-C_3N_4$  (air) when the incident light is located between 430 and 521 nm. Then, the absorbance of the tubular  $g-C_3N_4$  continues to strengthen when the incident light increases its wavelength, and eventually, it becomes the strongest among the three samples, which is indicative of the enhanced light harvesting ability of tubular  $g-C_3N_4$  itself. The enhanced light harvesting ability of tubular  $g-C_3N_4$  can be attributed to the multiple light scattering/reflection effect in the inner cavity of tubular  $g-C_3N_4$  (Scheme S2A†).

The optical properties of  $g-C_3N_4$  tubes,  $Co_3S_4$ , and CC- $x$  ( $x = 10, 15, 20, 25, 30, 35$ ) were studied using UV-vis diffuse reflectance spectra, as shown in Fig. 5B. The absorption edges of all composite samples shifted to a longer wavelength compared with the tubular  $g-C_3N_4$ , and the absorbance of these composite samples was higher than that of  $g-C_3N_4$  tubes. The absorbance of the composite increases with an

increase in the  $Co_3S_4$  ultrafine nanoparticles loaded on the surface of  $g-C_3N_4$  tubes. As depicted in Scheme S2B,† the ultrafine  $Co_3S_4$  nanoparticles loaded on the surface of  $g-C_3N_4$  tubes can act as a mirror with a rough surface to scatter and reflect the incident light. The incident light can be scattered and repeatedly reflected among the ultrafine  $Co_3S_4$  nanoparticles. The light can also be reflected by the ultrafine  $Co_3S_4$  nanoparticles toward different directions, and the scattered and reflected light will eventually irradiate to the surface of  $g-C_3N_4$  tubes, which enhances the light harvesting ability of tubular  $g-C_3N_4$ , and this is the reason for the enhanced light absorbance of all composites. However, loading too many  $Co_3S_4$  nanoparticles on the surface of  $g-C_3N_4$  tubes will lead to a decrease in light absorbance because too many  $Co_3S_4$  nanoparticles will hinder the incident light from irradiating to the surface of tubular  $g-C_3N_4$  (Scheme S2C†).

## 2.3 Hydrogen evolution performance and stability

The photocatalytic  $H_2$  evolution performance of  $g-C_3N_4$ ,  $Co_3S_4$ , and CC- $x$  ( $x = 10, 15, 20, 25, 30, 35$ ) at pH 9 was evaluated and is shown as Fig. 6A. The photocatalytic hydrogen evolution of tubular  $g-C_3N_4$  is  $12 \mu\text{mol g}^{-1} \text{ h}^{-1}$ . When the ultrafine  $Co_3S_4$  nanoparticles are anchored on the surface of  $g-C_3N_4$  tubes, the photocatalytic hydrogen evolution drastically increases. The photocatalytic hydrogen evolution of CC-25 is  $2120 \mu\text{mol g}^{-1} \text{ h}^{-1}$ , which is 176 times higher than that of pure tubular  $g-C_3N_4$ . The photocatalytic hydrogen evolution of CC-25 at different pH values was carried out, and the results are shown in Fig. 6B, from which it can be seen that the highest hydrogen evolution performance occurred at pH 9, which is indicative that it is an appropriate pH value that is suitable for hydrogen evolution. The hydrogen evolution of CC-25 decreases when the pH value is higher than 9, which likely occurs due to the decreased concentration of  $H^+$ , and thus, a decreased thermodynamic driving force for hydrogen evolution. It also was likely due to the strengthened electrostatic repulsion forces between the deprotonated EY and the negatively charged  $g-C_3N_4$  tubes. However, lowering the pH to 8 also leads to a decrease in the hydrogen evolution of CC-25, and the  $H_2$  evolution performance is drastically decreased when the pH value is lowered to 5. This can be explained in that an overly acidic environment will result in the protonation of triethanolamine (TEOA). Then, TEOA becomes an ineffective electron donor, and as a consequence, the  $H_2$  evolution performance decreases. Fig. 6C shows the  $H_2$  evolution performance of CC-25 in different sacrificial reagents, including 10% lactic acid,  $Na_2S/Na_2SO_3$  (0.35 M/0.25 M), 15% methanol, and 15% TEOA (pH 9). The photocatalytic activity of CC-25 in 15% TEOA (pH 9) in the presence of EY is the highest and is far beyond that of other sacrificial reagents, demonstrating that the composite catalyst CC-25 is selective of sacrificial reagents, and 15% TEOA (pH 9) is the most suitable for photocatalytic  $H_2$  evolution among these four

**Table 1** Parameters of physical adsorption

Samples	$S_{BET}$ , <sup>a</sup> $\text{m}^2 \text{ g}^{-1}$	Pore volume, <sup>b</sup> $\text{cm}^3 \text{ g}^{-1}$	Average pore size, <sup>b</sup> nm
$g-C_3N_4$	29	0.09	15
$Co_3S_4$	11	0.06	27
CC-25	22	0.09	27

<sup>a</sup> Obtained from the BET method. <sup>b</sup> Relative pressure ( $P/P_0$ ) was 0.99.

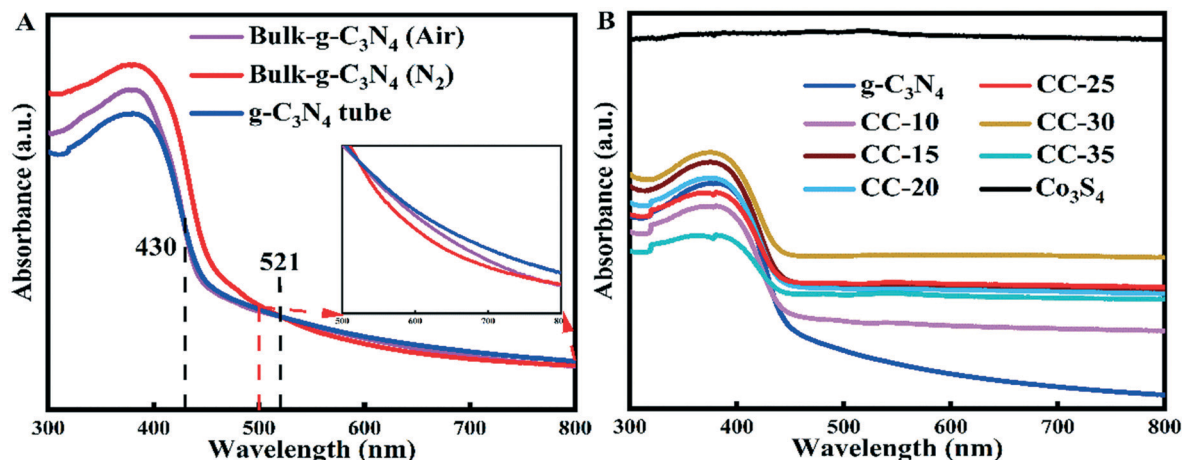


Fig. 5 UV-vis diffuse reflectance spectra of (A) g-C<sub>3</sub>N<sub>4</sub> (prepared under different conditions), (B) g-C<sub>3</sub>N<sub>4</sub> tubes, Co<sub>3</sub>S<sub>4</sub>, and CC-x (x = 10, 15, 20, 25, 30, 35).

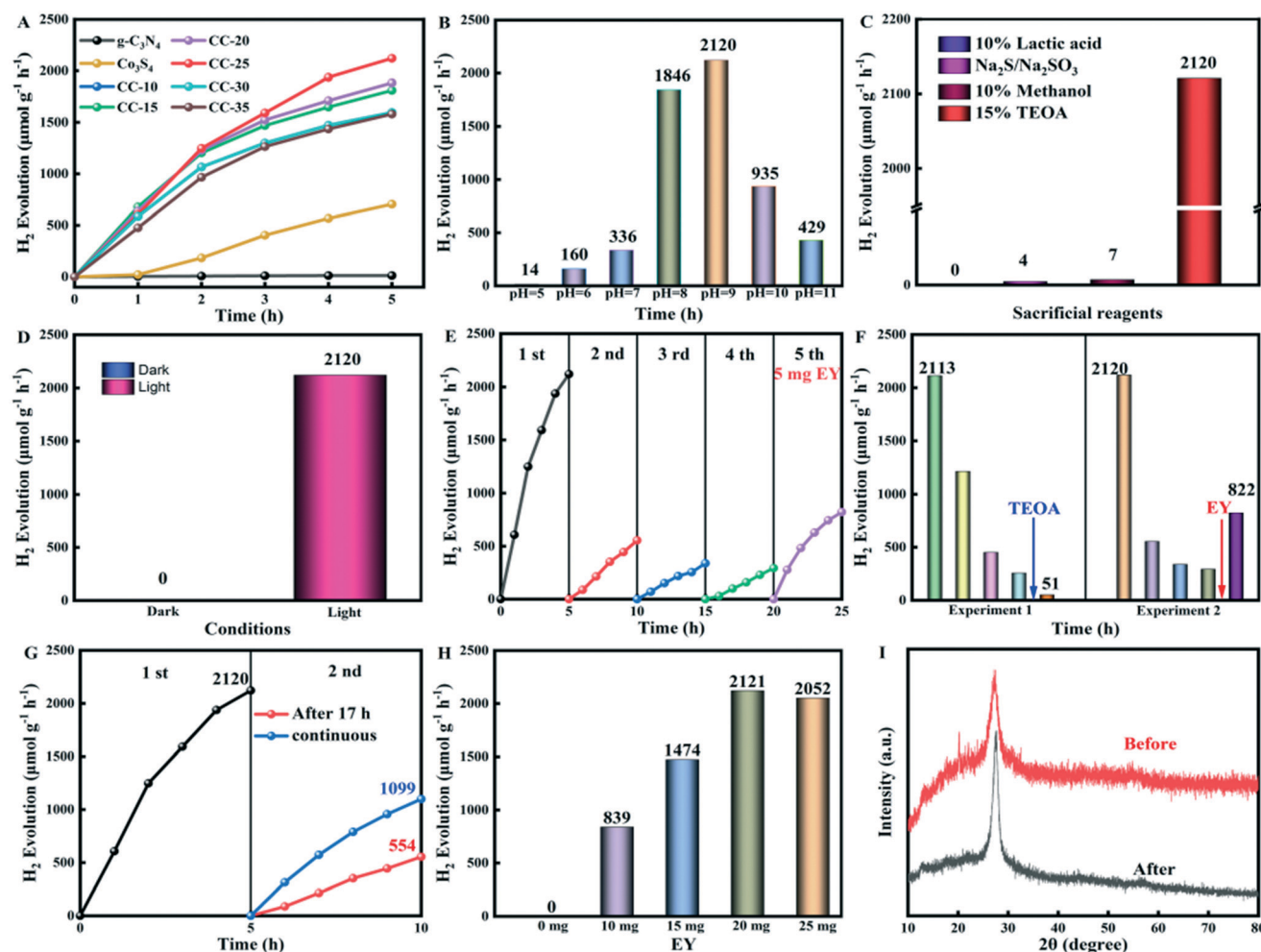


Fig. 6 (A) H<sub>2</sub> evolution of g-C<sub>3</sub>N<sub>4</sub>, Co<sub>3</sub>S<sub>4</sub>, and CC-10, CC-15, CC-20, CC-25, CC-30, and CC-35 within 5 h. (B) H<sub>2</sub> evolution of CC-25 at different pH values. (C) H<sub>2</sub> evolution of CC-25 in 10% lactic acid, Na<sub>2</sub>S/Na<sub>2</sub>SO<sub>3</sub> (0.35 M/0.25 M), 15% methanol, and TEOA (pH 9). (D) H<sub>2</sub> evolution of CC-25 under visible light and in the dark. (E) H<sub>2</sub> evolution stability test of CC-25. (F) Comparative experiments to study the fifth run by changing sacrificial reagents or adding EY. (G) Comparison of H<sub>2</sub> evolution stability test of CC-25 in the first and second runs when continuous and when 17 h apart. (H) H<sub>2</sub> evolution of CC-25 when adding different amounts of EY, (I) XRD patterns of CC-25 before and after the photocatalytic hydrogen evolution.

sacrificial reagents. EY was added to the system as a sensitizer to enhance the photocatalytic hydrogen evolution

activity of CC-25. TEOA (15%), as the sacrificial reagent, not only can consume photogenerated holes at the valence band

of  $g\text{-C}_3\text{N}_4$  tubes, but it also provides electrons for the transformation of EY from the triplet excited state ( $\text{EY}^{3*}$ ) to the transition state ( $\text{EY}^-$ ), and at last, the transition state EY can provide electrons to photocatalysts to participate in the  $\text{H}_2$  evolution reaction. For the other three sacrificial reagents, they can act as hole consumers instead of playing the role of electron donor to provide electrons to EY for its transformation between different excited states. Therefore, the photocatalytic hydrogen evolution of CC-25 in TEOA is much higher than that in other three sacrificial reagents. The hydrogen evolution of CC-25 in the dark and under the irradiation of visible light conditions was performed and is presented in Fig. 6D. There was no  $\text{H}_2$  produced when the lights were turned off, and it lasted for 5 h because electron-hole pairs cannot be excited.

The photocatalytic hydrogen evolution stability test of CC-25 was implemented in TEOA (pH 9) in the presence of EY, and the result is displayed in Fig. 6E. The hydrogen evolution performance of the composite catalyst was excellent in the first run, which lasted for 5 h. However, it drastically decreased when the test proceeded to the second run, and then decreased by inches in the third and the fourth runs. The drastic decrease in the second, third, and fourth runs compared with the first run can probably be attributed to two aspects. The sacrificial reagent (TEOA) in the reaction bottle was consumed because no extra TEOA was added to the reaction bottle. However, EY was degraded under the illumination of visible light in the presence of TEOA. Some extra experiments were conducted (presented in Fig. 6F) to confirm the proposed hypothesis above. In the first control experiment, the sacrificial reagent was changed in the fifth run but without adding any EY, and the hydrogen performance did not recover, but instead, continued to fall. In the second control experiment, five milligrams of EY were added to the reaction bottle in the fifth run without changing or adding the sacrificial reagent (TEOA). Then, the hydrogen evolution recovered, and it was almost 3 times higher than that of the fourth run. These results indicate that a drastic decrease in the photocatalytic hydrogen performance of CC-25 is not irrelevant to the consumption of TEOA. The hydrogen evolution performance of CC-25 in the stability test sharply decreased during the second run, which can probably be attributed to the degradation of EY under visible light because there was an interval of 17 h between the first and second runs. A control experiment was carried out to clarify what we surmised above, and the result is displayed in Fig. 6G. The hydrogen performance of CC-25 at the second run decreased almost 74% from 2120 to 554 when there was an interval of 17 h between the first and the second runs. However, the hydrogen performance of CC-25 at the second run only decreased 49% from 2120 to 1099 when the second run was carried out immediately after the first run. These results indicate that the drastic decrease in the hydrogen evolution performance of CC-25 is attributed to the degradation of EY. Also, Fig. 6I shows the XRD patterns of CC-25 before and after the photocatalytic hydrogen evolution

stability tests were conducted, and there is no obvious shift in characteristic peaks, which indicates that the composite is stable. The SEM image of CC-25 after photocatalytic hydrogen evolution was implemented is shown in Fig. S4,<sup>†</sup> which also confirms the stability of the composite. Fig. 6H shows the experiment where different amounts of EY were added to the reaction system to determine the most suitable amount for photocatalytic hydrogen evolution. No  $\text{H}_2$  can be produced when the amount of EY is 0 mg. Then, the hydrogen evolution increases with increasing amounts of added EY, but hydrogen performance decreases when excessive amounts of EY were added to the system. When the amount of EY is insufficient, it cannot provide enough electrons for the hydrogen evolution reaction. Conversely, excessive EY in the reaction system will create a shielding effect that is not beneficial for the hydrogen evolution reaction.

#### 2.4 Transfer kinetics of charges

The transfer kinetics of photo-generated charge carriers were studied by obtaining photoluminescence (PL) and time-resolved photoluminescence (TRPL) spectra, transient photocurrent response (IT) and electrochemical impedance (EIS) spectra, and linear scan voltammetry (LSV) spectra (Fig. 7). The intensity of the fluorescence can reflect the recombination rate of the electron-hole pairs because the recombination of photo-induced electron-hole pairs will emit fluorescence, and the fluorescence can be recorded. As depicted in Fig. 7A, the EY solution ( $1 \times 10^{-6} \text{ mol L}^{-1}$ ) exhibits a typical emission peak at approximately 540 nm when excited at 480 nm, being assigned to the conjugated xanthene structure with severe recombination of photogenerated electron-hole pairs. However, the emission peaks of EY-sensitized  $g\text{-C}_3\text{N}_4$ ,  $\text{Co}_3\text{S}_4$ , and CC-25 exhibited a blueshift compared with pristine EY, which can be attributed to the strong interaction that occurred between EY and each pristine sample. The intensity of the emission peak decreased when tubular  $g\text{-C}_3\text{N}_4$  was added to EY solution, and that of EY-sensitized  $\text{Co}_3\text{S}_4$  ultrafine nanoparticles decreased to a lower status, which revealed that photogenerated electrons from  $\text{EY}^*$  are easily transferred to  $\text{Co}_3\text{S}_4$  nanoparticles. The estimated potential of  $\text{EY}^*$  ( $-3.45 \text{ eV}$ )<sup>43</sup> is more negative than that of the conduction bands of tubular  $g\text{-C}_3\text{N}_4$  ( $-1.02 \text{ eV}$ ) and  $\text{Co}_3\text{S}_4$  ( $-1.41 \text{ eV}$ ) ultrafine nanoparticles, which creates a difference in the energy levels, and this enables electrons to be transferred from EY to  $g\text{-C}_3\text{N}_4$  tubes and  $\text{Co}_3\text{S}_4$  nanoparticles. Additionally, the PL intensity of CC-25 tested in EY aqueous solution further decreased compared to pristine  $g\text{-C}_3\text{N}_4$  after introducing  $\text{Co}_3\text{S}_4$  ultrafine nanoparticles. This indicated that electrons from the photoexcited  $\text{EY}^*$  can be separated and transferred to  $g\text{-C}_3\text{N}_4$  tubes and  $\text{Co}_3\text{S}_4$  nanoparticles, which resulted in PL quenching of EY. Fig. 7B shows that the photocurrent intensity of CC-25 was the lowest among the three samples, demonstrating that EY-sensitized CC-25 exhibited the lowest recombination rate of photogenerated electron-hole pairs. A more efficient transfer and separation can be obtained by introducing  $\text{Co}_3\text{S}_4$  ultrafine



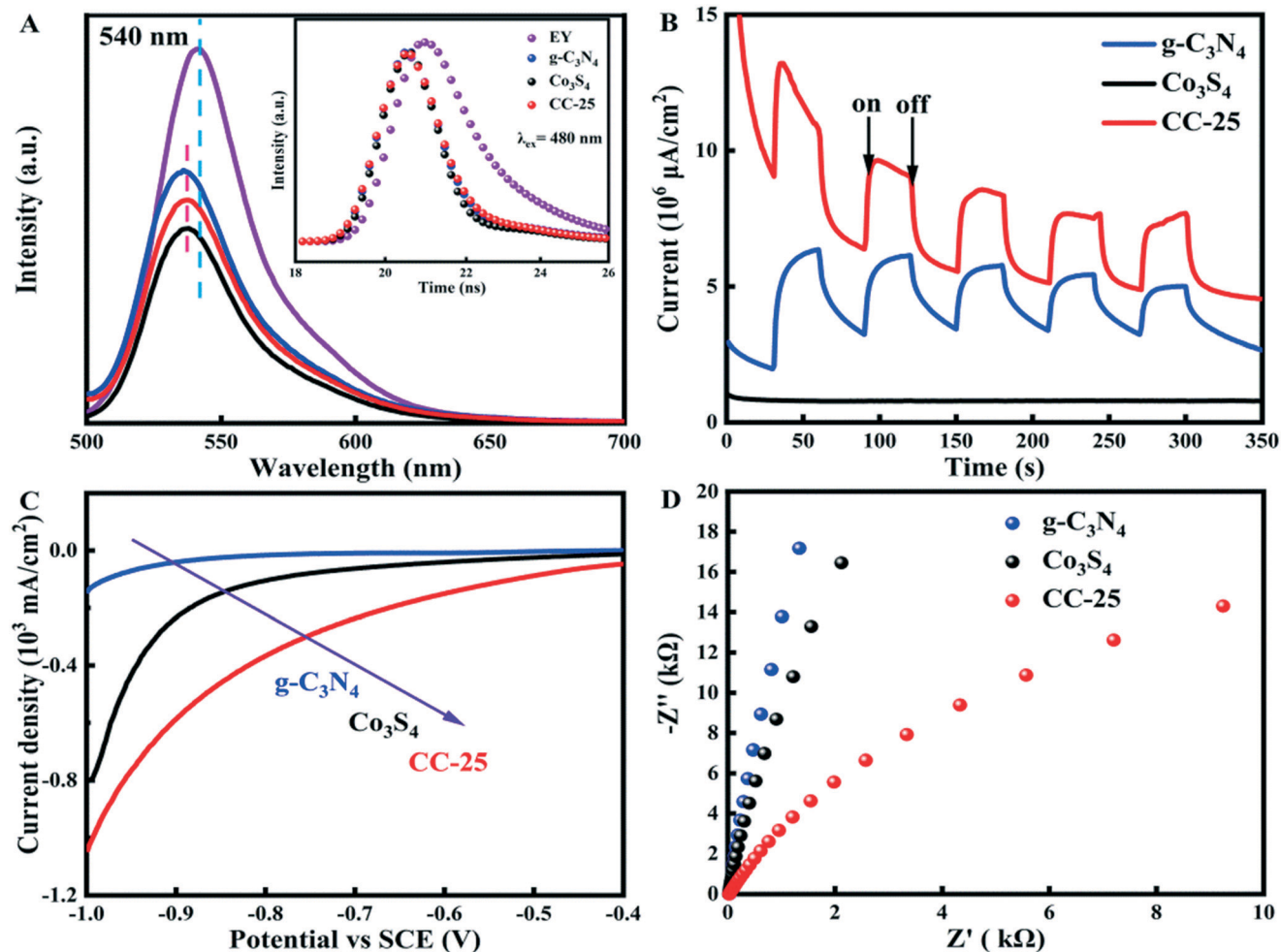


Fig. 7 (A) Photoluminescence (PL) spectroscopy of g-C<sub>3</sub>N<sub>4</sub>, Co<sub>3</sub>S<sub>4</sub>, and CC-25 (the inset image is time-resolved photoluminescence (TRPL)). (B) Photocurrent intensity of g-C<sub>3</sub>N<sub>4</sub>, Co<sub>3</sub>S<sub>4</sub>, and CC-25. (C) Linear scan voltammetry (LSV) of g-C<sub>3</sub>N<sub>4</sub>, Co<sub>3</sub>S<sub>4</sub>, and CC-25. (D) Nyquist plots of electrochemical impedance spectroscopy (EIS) of g-C<sub>3</sub>N<sub>4</sub>, Co<sub>3</sub>S<sub>4</sub>, and CC-25.

nanoparticles to form heterojunctions with tubular g-C<sub>3</sub>N<sub>4</sub>. The polarization curves of CC-25 (Fig. 7C) exhibited the lowest onset potential among these three samples, revealing an excellent performance in lowering the H<sub>2</sub>-evolution overpotential. In addition, the electrochemical impedance spectroscopy (Fig. 7D) of CC-25 carried out in 0.2 M Na<sub>2</sub>SO<sub>4</sub> solution showed a lower arc radius compared with those of pristine g-C<sub>3</sub>N<sub>4</sub> tubes and Co<sub>3</sub>S<sub>4</sub> ultrafine nanoparticles, which indicated that the introduction of Co<sub>3</sub>S<sub>4</sub> accelerated the transfer and separation of electrons between these two components, thus promoting photocatalytic hydrogen evolution. The enhanced transfer and separation of photogenerated charge carriers leads to additional electrons that can be utilized in the hydrogen evolution reaction (Table 2).

## 2.5 Band structure

The UV-vis diffuse reflectance spectra of g-C<sub>3</sub>N<sub>4</sub>, Co<sub>3</sub>S<sub>4</sub>, and CC-25 (Fig. 8A) show that the absorption edge and absorbance of CC-25 shift toward larger wavelengths and

become stronger after coupling with Co<sub>3</sub>S<sub>4</sub> ultrafine nanoparticles and g-C<sub>3</sub>N<sub>4</sub> tubes. Fig. 8B and C show the band gaps of g-C<sub>3</sub>N<sub>4</sub> tubes and Co<sub>3</sub>S<sub>4</sub> nanoparticles, and Fig. 8D shows the Mott-Schottky curves of g-C<sub>3</sub>N<sub>4</sub> tubes and Co<sub>3</sub>S<sub>4</sub> nanoparticles. It is well known that the conduction band of an n-type semiconductor is more negative by approximately -0.2 or -0.1 eV than its flat band.<sup>44,45</sup> Hence, the conduction bands of g-C<sub>3</sub>N<sub>4</sub> and Co<sub>3</sub>S<sub>4</sub> were calculated to be -1.26 and -1.65 V vs. SCE (saturate calomel electrode), and the conduction bands of these two components can also be presented as -1.02 and -1.41 V vs. NHE (normal hydrogen

Table 2 Parameters of emission decay of EY, g-C<sub>3</sub>N<sub>4</sub>, Co<sub>3</sub>S<sub>4</sub>, and CC-25

Samples	$\tau_1$ , <sup>a</sup> ns	$\tau_2$ , ns	$\tau_{\text{av}}$ , ns	$\chi^2$
EY	0.99 ( $B_1$ : 64.27%)	1.78 ( $B_2$ : 35.73%)	1.17	1.31
g-C <sub>3</sub> N <sub>4</sub>	0.43 ( $B_1$ : 91.37%)	4.92 ( $B_2$ : 8.63%)	0.47	1.48
Co <sub>3</sub> S <sub>4</sub>	4.42 ( $B_1$ : 5.19%)	0.32 ( $B_2$ : 94.81%)	0.33	1.45
CC-25	0.49 ( $B_1$ : 93.76%)	4.77 ( $B_2$ : 6.24%)	0.53	1.46

<sup>a</sup>  $\tau$ : Lifetime. <sup>b</sup>  $B$ : pre-exponential factor.

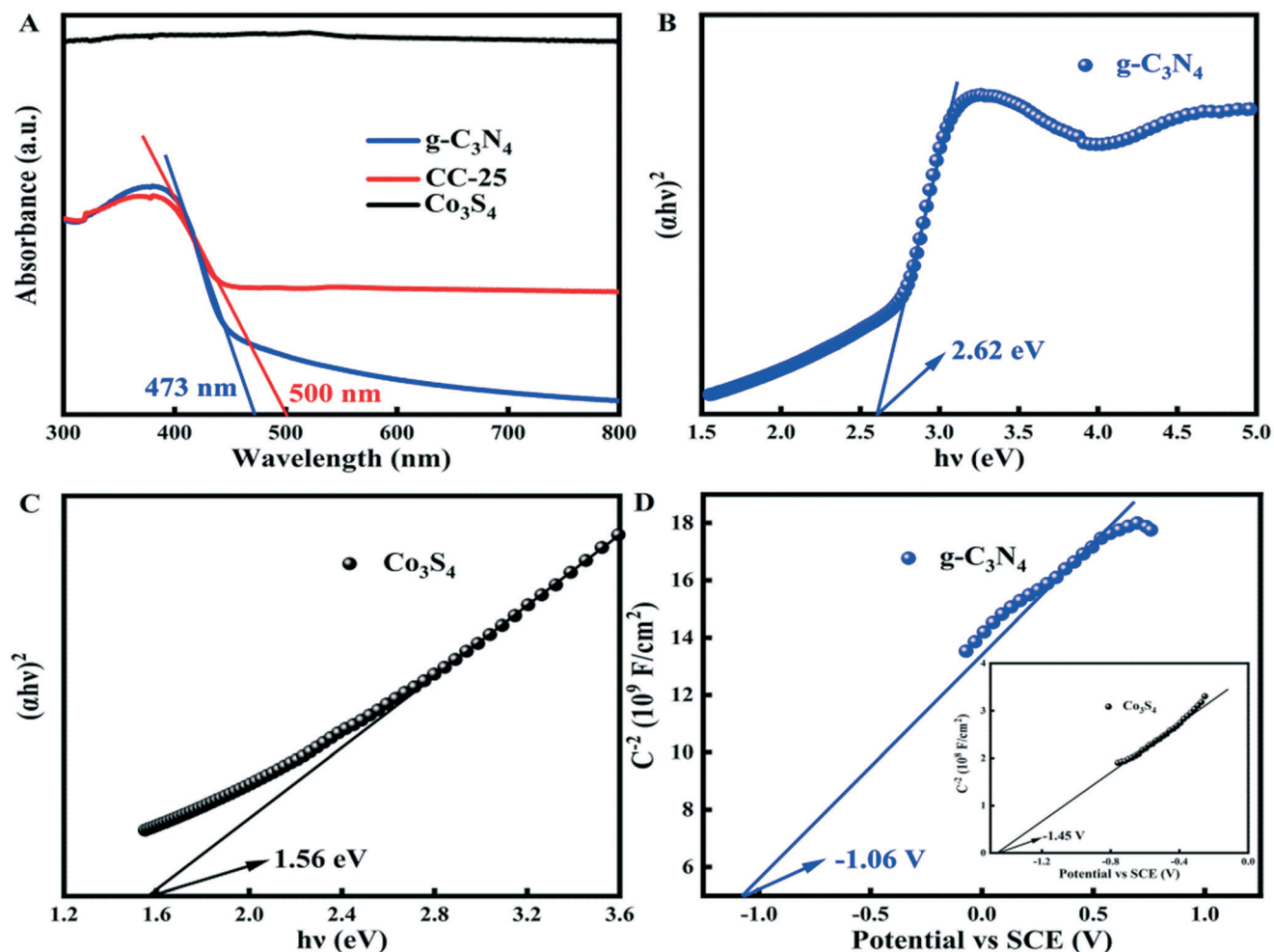


Fig. 8 (A) UV-vis diffuse reflectance spectra of g-C<sub>3</sub>N<sub>4</sub>, Co<sub>3</sub>S<sub>4</sub>, and CC-25. The corresponding plots of  $(\alpha hv)^2$  versus  $hv$  of (B) g-C<sub>3</sub>N<sub>4</sub> tubes and (C) Co<sub>3</sub>S<sub>4</sub>. (D) Mott-Schottky curves of g-C<sub>3</sub>N<sub>4</sub> and Co<sub>3</sub>S<sub>4</sub> (inset curve).

electrode) ( $E_{\text{NHE}} = E_{\text{SCE}} + 0.241 \text{ V}$ ).<sup>46–48</sup> In addition, the valance band of g-C<sub>3</sub>N<sub>4</sub> and Co<sub>3</sub>S<sub>4</sub> was determined to be 1.6 and 0.15 V by the equation:  $E_{\text{VB}} = E_{\text{CB}} + E_{\text{g}}$ .

## 2.6 Reaction mechanism

The light-harvesting performance of tubular g-C<sub>3</sub>N<sub>4</sub> can be enhanced through the multiple scatter/reflection effect that occurs in the inner cavity of g-C<sub>3</sub>N<sub>4</sub>. Additionally, the amorphous Co<sub>3</sub>S<sub>4</sub> ultrafine nanoparticles anchored on the outside surface of g-C<sub>3</sub>N<sub>4</sub> tubes can act as a mirror to scatter and reflect light, thus enhancing the light-harvesting performance of the composite catalyst. A possible mechanism for the photocatalytic hydrogen evolution is proposed (Fig. 9) to more optimally understand the entire process of photocatalysis based on all the results discussed in the above sections. Singlet excited states of EY<sup>1\*</sup> can be produced after absorbing light by EY, and then, the singlet excited states will produce triplet excited states EY<sup>3\*</sup> through fast intersystem crossing (ISC).<sup>49</sup> The triplet excited states EY<sup>3\*</sup> are reductively quenched when TEOA is added to the

system, producing EY<sup>•-</sup>. Electrons from EY<sup>•-</sup> can be transferred to the conduction bands of the Co<sub>3</sub>S<sub>4</sub> ultrafine nanoparticles and g-C<sub>3</sub>N<sub>4</sub> tubes, and at the same time, parts

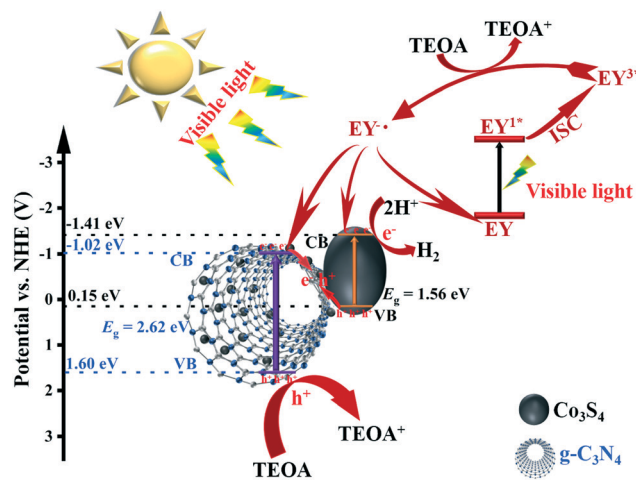


Fig. 9 Proposed mechanism for enhanced photocatalytic H<sub>2</sub> evolution under visible light irradiation.

of  $EY^-$  return to the ground state. Additionally,  $g-C_3N_4$  itself can be excited by absorbing light with energy that exceeds its band gap. Then, electron-hole pairs are excited, and electrons are later transferred to the conduction band (CB) of  $g-C_3N_4$  tubes.  $Co_3S_4$  ultra-fine nanoparticles can also be excited by visible light in a process similar to that which  $g-C_3N_4$  tubes undergo. Electrons from the CB of  $g-C_3N_4$  tubes and holes from the valence band (VB) of  $Co_3S_4$  ultrafine nanoparticles recombine in the interface after these two semiconductors are excited by visible light, and through this, the recombination rate of electron-hole pairs in both of the materials is reduced. The solid-solid contact between these two materials forms a "Step-scheme" transfer route between them, in which electrons from the CB of  $g-C_3N_4$  and holes from the VB of  $Co_3S_4$  recombine in their interface. For  $g-C_3N_4$  tubes, electrons are excited and transferred to its CB, and then subsequently transferred to the VB of  $Co_3S_4$  to recombine with photoexcited holes. For  $Co_3S_4$ , photoexcited holes are consumed by electrons from the CB of  $g-C_3N_4$ , and electrons are transferred to the CB where  $H_2$  is produced.

### 3. Conclusion

In summary, we successfully synthesized a heterojunction composed of ultrafine  $Co_3S_4$  nanoparticles on  $g-C_3N_4$  tubes. The light harvesting of  $g-C_3N_4$  was enhanced due to the scatter and reflect effect in the inner cavity of the  $g-C_3N_4$  tubes. The introduced  $Co_3S_4$  ultrafine nanoparticles act as a mirror to repeatedly scatter and reflect incident light, which enhances light utilization. The composite catalyst performed a photocatalytic hydrogen evolution activity that was significantly improved (176 times) compared with pristine  $g-C_3N_4$  tubes in the visible light region. Such a significant improvement in the performance of photocatalytic  $H_2$  production can be attributed to the formation of a step-scheme heterojunction between the two materials. This work will provide guidance for studying the step-scheme photocatalysts.

### Author contributions

Yuanpeng Wang and Xuqiang Hao designed the experiments, Zhiliang Jin and Tiansheng Zhao contributed reagents/materials and analysis tools, and Yuanpeng Wang and Lijun Zhang wrote the paper.

### Conflicts of interest

The authors declare that they have no conflicts of interest.

### Acknowledgements

This work was financially supported by the Natural Science Foundation of the Ningxia Hui Autonomous Region (2020AAC03204 and 2020AAC03208 and 2020AAC02026), the Open Project of State Key Laboratory of High-efficiency Utilization of Coal and Green Chemical Engineering, Ningxia University (2019-KF-36).

## References

- 1 L. Yin, S. Wang, C. Yang, S. Lyu and X. Wang, Modulation of Polymeric Carbon Nitrides through Supramolecular Preorganization for Efficient Photocatalytic Hydrogen Generation, *ChemSusChem*, 2019, **12**, 3320–3325.
- 2 J. Fu, Q. Xu, J. Low, C. Jiang and J. Yu, Ultrathin 2D/2D  $WO_3/g-C_3N_4$  step-scheme  $H_2$ -production photocatalyst, *Appl. Catal., B*, 2019, **243**, 556–565.
- 3 X. Meng, C. Zhang, C. Dong, W. Sun, D. Ji and Y. Ding, Carbon quantum dots assisted strategy to synthesize  $Co@NC$  for boosting photocatalytic hydrogen evolution performance of CdS, *Chem. Eng. J.*, 2020, **389**, 124432.
- 4 M. Zhang, Q. Hu, K. Ma, Y. Ding and C. Li, Pyroelectric effect in CdS nanorods decorated with a molecular Co-catalyst for hydrogen evolution, *Nano Energy*, 2020, **73**, 104810.
- 5 H. Gong, Z. Li, Z. Chen, Q. Liu, M. Song and C. Huang, NiSe/ $Cd_{0.5}Zn_{0.5}S$  Composite Nanoparticles for Use in p-n Heterojunction-Based Photocatalysts for Solar Energy Harvesting, *ACS Appl. Nano Mater.*, 2020, **3**, 3665–3674.
- 6 Z. Chen, H. Gong, Q. Liu, M. Song and C. Huang, NiSe<sub>2</sub> Nanoparticles Grown in Situ on CdS Nanorods for Enhanced Photocatalytic Hydrogen Evolution, *ACS Sustainable Chem. Eng.*, 2019, **7**, 16720–16728.
- 7 Y. Li, H. Li, Y. Li, S. Peng and Y. H. Hu, Fe-B alloy coupled with Fe clusters as an efficient cocatalyst for photocatalytic hydrogen evolution, *Chem. Eng. J.*, 2018, **344**, 506–513.
- 8 Y. Li, Z. Jin, L. Zhang and K. Fan, Controllable design of Zn-Ni-P on  $g-C_3N_4$  for efficient photocatalytic hydrogen production, *Chin. J. Catal.*, 2019, **40**, 390–402.
- 9 T. Jia, F. Fu, J. Li, Z. Deng, F. Long, D. Yu, Q. Cui and W. Wang, Rational construction of direct Z-scheme SnS/ $g-C_3N_4$  hybrid photocatalyst for significant enhancement of visible-light photocatalytic activity, *Appl. Surf. Sci.*, 2020, **499**, 143941.
- 10 T. Jia, F. Fu, D. Yu, J. Cao and G. Sun, Facile synthesis and characterization of N-doped  $TiO_2/C$  nanocomposites with enhanced visible-light photocatalytic performance, *Appl. Surf. Sci.*, 2018, **430**, 438–447.
- 11 T. Jia, F. Fu, J. Li, W. Wang and X. Hu, Constructing a novel  $Zn_2SnO_4/C/AgBr$  nanocomposite with extended spectral response and improved photocatalytic performance, *J. Alloys Compd.*, 2019, **783**, 687–696.
- 12 L. Su, L. Luo, H. Song, Z. Wu, W. Tu, Z.-j. Wang and J. Ye, Hemispherical shell-thin lamellar  $WS_2$  porous structures composited with CdS photocatalysts for enhanced  $H_2$  evolution, *Chem. Eng. J.*, 2020, **388**, 124346.
- 13 F. Yang, D. Liu, Y. Li, L. Cheng and J. Ye, Lithium incorporation assisted synthesis of ultra-small  $Mo_2C$  nanodots as efficient photocatalytic  $H_2$  evolution cocatalysts, *Chem. Eng. J.*, 2020, **399**, 125794.
- 14 H. Lin, K. Zhang, G. Yang, Y. Li, X. Liu, K. Chang, Y. Xuan and J. Ye, Ultrafine nano 1T- $MoS_2$  monolayers with NiOx as dual co-catalysts over  $TiO_2$  photoharvester for efficient photocatalytic hydrogen evolution, *Appl. Catal., B*, 2020, **279**, 119387.

- 15 Q. Xu, B. Zhu, B. Cheng, J. Yu, M. Zhou and W. Ho, Photocatalytic H<sub>2</sub> evolution on graphdiyne/g-C<sub>3</sub>N<sub>4</sub> hybrid nanocomposites, *Appl. Catal., B*, 2019, **255**, 117770.
- 16 Z. Jin, L. Zhang, G. Wang, Y. Li and Y. Wang, Graphdiyne formed a novel CuI-GD/g-C<sub>3</sub>N<sub>4</sub> S-scheme heterojunction composite for efficient photocatalytic hydrogen evolution, *Sustainable Energy Fuels*, 2020, **4**, 5088–5101.
- 17 Y. Li, H. Yang, G. Wang, B. Ma and Z. Jin, Distinctive Improved Synthesis and Application Extensions Graphdiyne for Efficient Photocatalytic Hydrogen Evolution, *ChemCatChem*, 2020, **12**, 1985–1995.
- 18 X. Li, J. Xiong, X. Gao, J. Ma, Z. Chen, B. Kang, J. Liu, H. Li, Z. Feng and J. Huang, Novel BP/BiOBr S-scheme nano-heterojunction for enhanced visible-light photocatalytic tetracycline removal and oxygen evolution activity, *J. Hazard. Mater.*, 2020, **387**, 121690.
- 19 X. Wang, K. Maeda, A. Thomas, K. Takanebe, G. Xin, J. M. Carlsson, K. Domen and M. Antonietti, A metal-free polymeric photocatalyst for hydrogen production from water under visible light, *Nat. Mater.*, 2008, **8**, 76–80.
- 20 H. Wang, X. Li and J. Yang, The g-C<sub>3</sub>N<sub>4</sub>/C<sub>2</sub>N Nanocomposite: A g-C<sub>3</sub>N<sub>4</sub>-Based Water-Splitting Photocatalyst with Enhanced Energy Efficiency, *ChemPhysChem*, 2016, **17**, 2100–2104.
- 21 Z. Zeng, H. Yu, X. Quan, S. Chen and S. Zhang, Structuring phase junction between tri-s-triazine and triazine crystalline C<sub>3</sub>N<sub>4</sub> for efficient photocatalytic hydrogen evolution, *Appl. Catal., B*, 2018, **227**, 153–160.
- 22 Z. You, Y. Su, Y. Yu, H. Wang, T. Qin, F. Zhang, Q. Shen and H. Yang, Preparation of g-C<sub>3</sub>N<sub>4</sub> nanorod/InVO<sub>4</sub> hollow sphere composite with enhanced visible-light photocatalytic activities, *Appl. Catal., B*, 2017, **213**, 127–135.
- 23 Q. Han, B. Wang, Y. Zhao, C. Hu and L. Qu, A Graphitic-C<sub>3</sub>N<sub>4</sub> “Seaweed” Architecture for Enhanced Hydrogen Evolution, *Angew. Chem., Int. Ed.*, 2015, **54**, 11433–11437.
- 24 Y. Li, R. Jin, Y. Xing, J. Li, S. Song, X. Liu, M. Li and R. Jin, Macroscopic Foam-Like Holey Ultrathin g-C<sub>3</sub>N<sub>4</sub> Nanosheets for Drastic Improvement of Visible-Light Photocatalytic Activity, *Adv. Energy Mater.*, 2016, **6**, 1601273.
- 25 Y. Li, M. Gu, T. Shi, W. Cui, X. Zhang, F. Dong, J. Cheng, J. Fan and K. Lv, Carbon vacancy in C<sub>3</sub>N<sub>4</sub> nanotube: Electronic structure, photocatalysis mechanism and highly enhanced activity, *Appl. Catal., B*, 2020, **262**, 118281.
- 26 S. Wan, M. Ou, Y. Wang, Y. Zeng, Y. Xiong, F. Song, J. Ding, W. Cai, S. Zhang and Q. Zhong, Protonic acid-assisted universal synthesis of defect abundant multifunction carbon nitride semiconductor for highly-efficient visible light photocatalytic applications, *Appl. Catal., B*, 2019, **258**, 118011.
- 27 D. Long, W. Chen, S. Zheng, X. Rao and Y. Zhang, Barium- and Phosphorus-Codoped g-C<sub>3</sub>N<sub>4</sub> Microtubes with Efficient Photocatalytic H<sub>2</sub> Evolution under Visible Light Irradiation, *Ind. Eng. Chem. Res.*, 2020, **59**, 4549–4556.
- 28 Y. Hong, L. Wang, E. Liu, J. Chen, Z. Wang, S. Zhang, X. Lin, X. Duan and J. Shi, A curly architected graphitic carbon nitride (g-C<sub>3</sub>N<sub>4</sub>) towards efficient visible-light photocatalytic H<sub>2</sub> evolution, *Inorg. Chem. Front.*, 2020, **7**, 347–355.
- 29 N. A. Wasio, R. C. Quardokus, R. P. Forrest, C. S. Lent, S. A. Corcelli, J. A. Christie, K. W. Henderson and S. A. Kandel, Self-assembly of hydrogen-bonded two-dimensional quasicrystals, *Nature*, 2014, **507**, 86–89.
- 30 T. Jordan, N. Fechner, J. Xu, T. J. K. Brenner, M. Antonietti and M. Shalom, “Caffeine Doping” of Carbon/Nitrogen-Based Organic Catalysts: Caffeine as a Supramolecular Edge Modifier for the Synthesis of Photoactive Carbon Nitride Tubes, *ChemCatChem*, 2015, **7**, 2826–2830.
- 31 J. Zhang, X. Chen, K. Takanebe, K. Maeda, K. Domen, J. D. Epping, X. Fu, M. Antonietti and X. Wang, Synthesis of a Carbon Nitride Structure for Visible-Light Catalysis by Copolymerization, *Angew. Chem., Int. Ed.*, 2010, **49**, 441–444.
- 32 H. Ye, Z. Wang, F. Yu, S. Zhang, K. Kong, X. Gong, J. Hua and H. Tian, Fluorinated conjugated poly(benzotriazole)/g-C<sub>3</sub>N<sub>4</sub> heterojunctions for significantly enhancing photocatalytic H<sub>2</sub> evolution, *Appl. Catal., B*, 2020, **267**, 118577.
- 33 Y. Chen, F. Su, H. Xie, R. Wang, C. Ding, J. Huang, Y. Xu and L. Ye, One-step construction of S-scheme heterojunctions of N-doped MoS<sub>2</sub> and S-doped g-C<sub>3</sub>N<sub>4</sub> for enhanced photocatalytic hydrogen evolution, *Chem. Eng. J.*, 2021, **404**, 126498.
- 34 M. Wu, J. Zhang, B.-b. He, H.-w. Wang, R. Wang and Y.-s. Gong, In-situ construction of coral-like porous P-doped g-C<sub>3</sub>N<sub>4</sub> tubes with hybrid 1D/2D architecture and high efficient photocatalytic hydrogen evolution, *Appl. Catal., B*, 2019, **241**, 159–166.
- 35 W. Li, Y. Li, C. Yang, Q. Ma, K. Tao and L. Han, Fabrication of 2D/2D nanosheet heterostructures of ZIF-derived Co<sub>3</sub>S<sub>4</sub> and g-C<sub>3</sub>N<sub>4</sub> for asymmetric supercapacitors with superior cycling stability, *Dalton Trans.*, 2020, **49**, 14017–14029.
- 36 V. Shrivastav, S. Sundriyal, P. Goel, V. Shrivastav, U. K. Tiwari and A. Deep, ZIF-67 derived Co<sub>3</sub>S<sub>4</sub> hollow microspheres and WS<sub>2</sub> nanorods as a hybrid electrode material for flexible 2V solid-state supercapacitor, *Electrochim. Acta*, 2020, **345**, 136194.
- 37 Z. Liang, S. Yang, X. Wang, H. Cui, X. Wang and J. Tian, The metallic 1T-phase WS<sub>2</sub> nanosheets as cocatalysts for enhancing the photocatalytic hydrogen evolution of g-C<sub>3</sub>N<sub>4</sub> nanotubes, *Appl. Catal., B*, 2020, **274**, 119114.
- 38 X. Han, D. Xu, L. An, C. Hou, Y. Li, Q. Zhang and H. Wang, Ni-Mo nanoparticles as co-catalyst for drastically enhanced photocatalytic hydrogen production activity over g-C<sub>3</sub>N<sub>4</sub>, *Appl. Catal., B*, 2019, **243**, 136–144.
- 39 J. Fu, C. Bie, B. Cheng, C. Jiang and J. Yu, Hollow CoSx Polyhedrons Act as High-Efficiency Cocatalyst for Enhancing the Photocatalytic Hydrogen Generation of g-C<sub>3</sub>N<sub>4</sub>, *ACS Sustainable Chem. Eng.*, 2018, **6**, 2767–2779.
- 40 C. Liang, X. Zhang, P. Feng, H. Chai and Y. Huang, ZIF-67 derived hollow cobalt sulfide as superior adsorbent for effective adsorption removal of ciprofloxacin antibiotics, *Chem. Eng. J.*, 2018, **344**, 95–104.
- 41 H. Yang, J. Yin, R. Cao, P. Sun, S. Zhang and X. Xu, Constructing highly dispersed 0D Co<sub>3</sub>S<sub>4</sub> quantum dots/2D g-C<sub>3</sub>N<sub>4</sub> nanosheets nanocomposites for excellent photocatalytic performance, *Sci. Bull.*, 2019, **64**, 1510–1517.

- 42 Y. Du, X. Zhu, X. Zhou, L. Hu, Z. Dai and J. Bao,  $\text{Co}_3\text{S}_4$  porous nanosheets embedded in graphene sheets as high-performance anode materials for lithium and sodium storage, *J. Mater. Chem. A*, 2015, **3**, 6787–6791.
- 43 S. Min and G. Lu, Enhanced Electron Transfer from the Excited Eosin Y to mpg- $\text{C}_3\text{N}_4$  for Highly Efficient Hydrogen Evolution under 550 nm Irradiation, *J. Phys. Chem. C*, 2012, **116**, 19644–19652.
- 44 Y. Wang, X. Hao, L. Zhang, Y. Li and Z. Jin, Rational Design of All-Solid-State 0D/2D  $\text{Mn}_{0.2}\text{Cd}_{0.8}\text{S}/\text{CeO}_2$  Direct Z-Scheme for Photocatalytic Hydrogen Evolution, *Energy Fuels*, 2020, **34**, 2599–2611.
- 45 L. Zhang, X. Hao, Y. Wang, Z. Jin and Q. Ma, Construction strategy of Mo-S@Mo-P heterojunction formed with in-situ phosphating Mo-S nanospheres toward efficient photocatalytic hydrogen production, *Chem. Eng. J.*, 2020, **391**, 123545.
- 46 Y. Wang, G. Wang, L. Zhang, Z. Jin and T. Zhao, Hydroxides  $\text{Ni}(\text{OH})_2$  &  $\text{Ce}(\text{OH})_3$  as a novel hole storage layer for enhanced photocatalytic hydrogen evolution, *Dalton Trans.*, 2019, **48**, 17660–17672.
- 47 X. Hao, J. Zhou, Z. Cui, Y. Wang, Y. Wang and Z. Zou, Zn-vacancy mediated electron-hole separation in  $\text{ZnS}/\text{g-C}_3\text{N}_4$  heterojunction for efficient visible-light photocatalytic hydrogen production, *Appl. Catal., B*, 2018, **229**, 41–51.
- 48 H. Liu, T. Yan, Z. Jin and Q. Ma, CoP nanoparticles as cocatalyst modified the  $\text{CdS}/\text{NiWO}_4$  p-n heterojunction to produce hydrogen efficiently, *New J. Chem.*, 2020, **44**, 1426–1438.
- 49 L. Yang, J. Huang, L. Shi, L. Cao, W. Zhou, K. Chang, X. Meng, G. Liu, Y. Jie and J. Ye, Efficient hydrogen evolution over Sb doped  $\text{SnO}_2$  photocatalyst sensitized by Eosin Y under visible light irradiation, *Nano Energy*, 2017, **36**, 331–340.